ACS APPLIED MATERIALS & INTERFACES

www.acsami.org

Research Article

Enhanced Response Speed in 2D Perovskite Oxides-Based Photodetectors for UV Imaging through Surface/Interface Carrier-Transport Modulation

Xinya Liu, Siyuan Li, Ziqing Li, Fa Cao, Li Su, Dmitry V. Shtansky, and Xiaosheng Fang*

Cite This: *ACS Appl. Mater. Interfaces* 2022, 14, 48936−48947

Read Online

ACCESS | Metrics & More | Article Recommendations | Supporting Information

ABSTRACT: The long-time decay process induced by the persistent photoconductivity (PPC) in metal oxides-based photodetectors (PDs) impedes our demands for high-speed photodetectors. 2D perovskite oxides, emerging candidates for future high-performance PDs, also suffer from the PPC effect. Here, by integrating 2D perovskite $Sr_2Nb_3O_{10}$ (SNO) nanosheets and nitrogen-doped graphene quantum dots (NGQDs), a unique nanoscale heterojunction is designed to modulate surface/interface carrier transport for enhanced response speed. Notably, the decay time is reduced from hundreds of seconds to a few seconds. The 4%NGQDs-SNO PD exhibits excellent performance with a photocurrent of 0.47 μA, a high on−off ratio of 2.2×10^4, and a fast pulse response speed (τ_{decay} = 67.3 ms), making it promising for UV imaging. The trap-involved decay process plays a dominant role in determining the decay time, resulting in the PPC effect in SNO PD, and the trap states mainly originate from oxygen vacancies and chemisorbed oxygen molecules. A significantly enhanced photoresponse speed in NGQDs-SNO PDs can be ascribed to the modulated surface/interface trap states and the efficient carrier pathway provided by the nanoscale heterojunction. This work provides an effective way to enhance the response speed in 2D perovskite oxides constrained by PPC via surface/interface engineering, promoting their applications in optoelectronics.

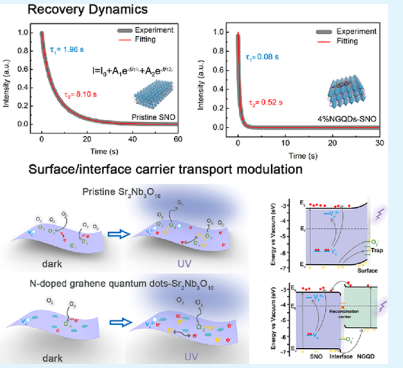

KEYWORDS: *perovskite oxides, photodetectors, persistent photoconductivity, trap states, enhanced response speed, surface/interface engineering*

1. INTRODUCTION

The light−matter interaction is crucial to the photoelectronic performance of photodetectors (PDs). The behavior of the photogenerated carriers can be tracked and resolved into four processes, including generation, separation, transportation, and extraction of the charge carriers.[1] The efficiency of the carrier transport can be greatly affected by the trap states in the semiconductor, which can dominate the lifetime of the photogenerated carriers and thereby alter the photodetecting performance.[2,3] The persistent photoconductivity (PPC) effect observed in metal oxide-based PDs is a typical case that the defect-related trap states can be a crucial interference factor in the behavior of photocarriers.[4,5]

Traditional wide-bandgap metal oxides such as ZnO, SnO_2, and Ga_2O_3 are ideal building blocks for PDs due to their high absorption coefficient in the ultraviolet band.[6,7] Nevertheless, a poor real-time response is found to be a common limitation of metal oxide photodetectors since the photocurrent typically requires a long time to recover to its initial value after switching off the light source, which is termed persistent photoconductivity (PPC).[8] Up to now, the origin of the PPC effect in metal oxides has been extensively studied. Two main mechanisms are proposed to describe the photocarrier dynamic under PPC effect. One is associated with the intrinsic defect-induced trap states. For example, the oxygen vacancy (V_o) in metal oxides is a typical structural defect that introduces shallow or deep traps within the bandgap. Upon illumination, the deep, neutral V_o states are ionized to shallow donor states V_o^{2+} and release two electrons, resulting in an increase in photoconductivity, while the neutralization of the V_o^{2+} states requires overcoming an energy barrier originating from the large lattice relaxation.[8−11] The other one emphasizes the effect of the surface trap states.[12−14] The adsorption and desorption of oxygen molecules can induce a high density of trap states at the surface of low-dimensional metal oxides, which promotes the separation of photogenerated pairs and the accumulation of trapped holes at the surface. Whether these PPC-related mechanisms coexist or which mechanism dominates the PPC phenomenon remains debatable and depends on the specific conditions.[15,16] But, it is clear that the

Received: September 7, 2022
Accepted: October 13, 2022
Published: October 23, 2022

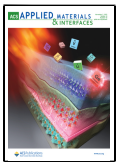

long lifetime of the photocarriers induced by trap states directly contributes to the PPC effect and influences the photodetecting performance.

Recently, perovskite materials have come to prominence in the field of PDs for the applications of light communication, wearable devices, electronic bionic eye, etc.,[17,18] due to their excellent optoelectronic properties, including large light absorption, high carrier mobility, and long carrier diffusion length.[19,20] 2D perovskite oxides (e.g., $Sr_2Nb_3O_{10}$, $Ca_2Nb_3O_{10}$, etc.) are promising candidates for UV photodetection in perovskite families. Ultrahigh responsivity can be achieved in the PD based on a single $Sr_2Nb_3O_{10}$ nanosheet, while the response speed is relatively slow with a tail-like decay curve.[21] Our further experiments show that PDs constructed from $Sr_2Nb_3O_{10}$ nanosheet films exhibit a higher photocurrent but an interior response speed with the decay time lasting hundreds of seconds, which can be regarded as the PPC effect. This indicates the probable presence of trap states in perovskite oxide nanosheets and it can be inferred from the material structure. Compared to halide perovskites, the presence of oxygen atoms endows perovskite oxides with some attractive properties but simultaneously introduces a certain number of oxygen vacancy defects.[22−25] In addition to intrinsic oxygen vacancies in the bulk phase, the exfoliation process would lead to comparable amounts of oxygen atoms escaping from the surface, which leaves surface oxygen vacancies in nanosheets.[26] Simultaneously, oxygen molecules prefer to be adsorbed at the oxygen vacancy site or other dangling bonds, thus the presence of abundant surface oxygen vacancies facilitates the oxygen adsorption/desorption process. Hence, for the photodetectors based on 2D perovskite oxides, exploring the relationship between the defect-induced trap states and photoelectric properties is of utmost importance for understanding and modulating the photodetecting performance.

To overcome the limitation of slow response speed, methods should be taken to block or eliminate the PPC effect in 2D perovskite oxides. Here, considering that PPC is largely affected by the surface states, surface/interface engineering could be a good choice to tune the photoelectronic properties of 2D materials with a high surface-to-volume ratio.[27,28] A large number of researches have utilized surface/interface engineering to realize high performance of semiconductor devices.[29−32] For instance, He and co-workers designed an ohmic junction between MXene and silicon surface to suppress the charge carrier recombination for optimizing the efficiency of solar cells.[33] In the field of photodetectors, in order to modulate photoresponse, many novel devices regulated the photogenerated carriers by constructing surface nanostructures, lattice-matched heterojunctions, van der Waals heterojunctions, etc.[34] Among these strategies, constructing nanoscale surface heterojunctions via integrating 0D nanomaterials has been proven to be effective and nondestructive. Various 0D materials, such as $CsPbBr_3$ quantum dots, HgTe nanocrystals, and PbS quantum dots, were hybridized with low-dimensional metal oxides to modulate the surface/interface charge behavior and optimize the photodetector performance. Due to the intriguing interfacial charge transfer behavior, the mixed dimensional heterojunction has shown fascinating properties beyond the individual metal oxides.[35−37] The decoration of 0D materials also changes the condition of the exposed material surface, thereby influencing the interaction of the photocarriers with chemisorbed foreign atoms or molecules.[28,38] Nitrogen-doped graphene quantum dots (NGQDs), an attractive carbon material, have extraordinary optical and electrical characteristics due to their pronounced quantum confinement and edge effects. The electron-rich nitrogen atoms endow NQGDs with extensive delocalized electrons and high charge carrier density, making them more favorable for potential optoelectronic devices.[39−41] NGQDs have been reported to exhibit superior electron transfer/reservoir properties when incorporated into metal oxides, resulting in the high sensing performance of the hybrid structure.[42−45] Moreover, compared with 0D materials mentioned above, NGQDs have the advantages of low toxicity, high chemical stability, and low cost.[46] Therefore, NGQDs are suitable building blocks for constructing nanoscale heterojunctions with 2D perovskite oxides, and the surface/interface charge carrier behavior in this hybrid structure remains to be explored.

Herein, we focus on improving the photoresponse speed of 2D perovskite oxides-based PDs. By integrating 2D perovskite SNO nanosheets and NGQDs, a unique nanoscale heterojunction is designed to suppress PPC effect and enhance response speed. For the pristine SNO PD, a certain number of oxygen vacancies and adsorbed oxygen molecules induce an ultralong recovery time of ∼120 s. In comparison, NGQDs-SNO PDs exhibit varying degrees of improvement in the response speed as the contents of NGQDs changes. Notably, the decay time can be shortened from hundreds of seconds to a few seconds. The 4%NGQDs-SNO PD achieves a high photocurrent of 0.47 μA, a high on−off ratio of 2.2×10^4, and a fast pulse response speed (τ_{decay} = 67.3 ms), which makes it promising for UV imaging sensors. Quantified relaxation dynamics data combined with density functional theory (DFT) calculations confirm that oxygen vacancies and adsorbed oxygen molecules introduce trap states, which play a dominant role in prolonging the decay time in the pristine SNO PD. The incorporation of NGQDs modulates the surface/interface carrier transport by minimizing the interaction between photocarriers and chemisorbed oxygen molecules, and providing an efficient carrier pathway through the formed nanoscale heterojunction. This work provides an effective strategy for the response speed enhancement of 2D perovskite oxides suffering from the PPC effect via surface/interface engineering.

2. EXPERIMENTAL SECTION

Preparation of the NGQDs-SNO Samples. The preparation of the SNO nanosheets was performed by combining high-temperature calcination and subsequent liquid exfoliation process. The calcination process consisted of two steps. A mixture of Cs_2CO_3 (99.99%), Sr_2CO_3 (99.99%), and Nb_2O_5 (99.99%) with a molar ratio of Cs/Sr/Nb = 1.2:2:3 was thoroughly ground and calcined at 1100 °C for 10 h in air, and then, the excess Cs_2CO_3 (5 mol %) was compensated for the next step calcination at 1350 °C for another 10 h in air. The obtained layered $CsSr_2Nb_3O_{10}$ precursor was stirred in 2 M HCl for 4 days to replace Cs ions with protons. The powder was then washed thoroughly with DI water and dried at 80 °C in air. Subsequently, the intermediate product $HSr_2Nb_3O_{10}$ was dispersed in 50 mL of an aqueous solution containing an equimolar amount of tera(*n*-butyl) ammonium hydroxide (TBAOH), and the solution was mechanically shaken for more than 1 week to obtain the SNO nanosheets. The nanosheets were washed by centrifugation and redispersed in 30 mL of water. NGQDs were synthesized though a hydrothermal method. Citric acid (1.68 g) and urea (1.44 g) were dissolved in 40 mL of DI water. After being stirred for 5 min, the clear solution was transferred into a 50 mL Teflon-lined stainless autoclave, heated to 180 °C in 20 min, and kept for 8 h. The obtained yellow solution of NGQDs was

https://doi.org/10.1021/acsami.2c15946
ACS Appl. Mater. Interfaces 2022, 14, 48936−48947

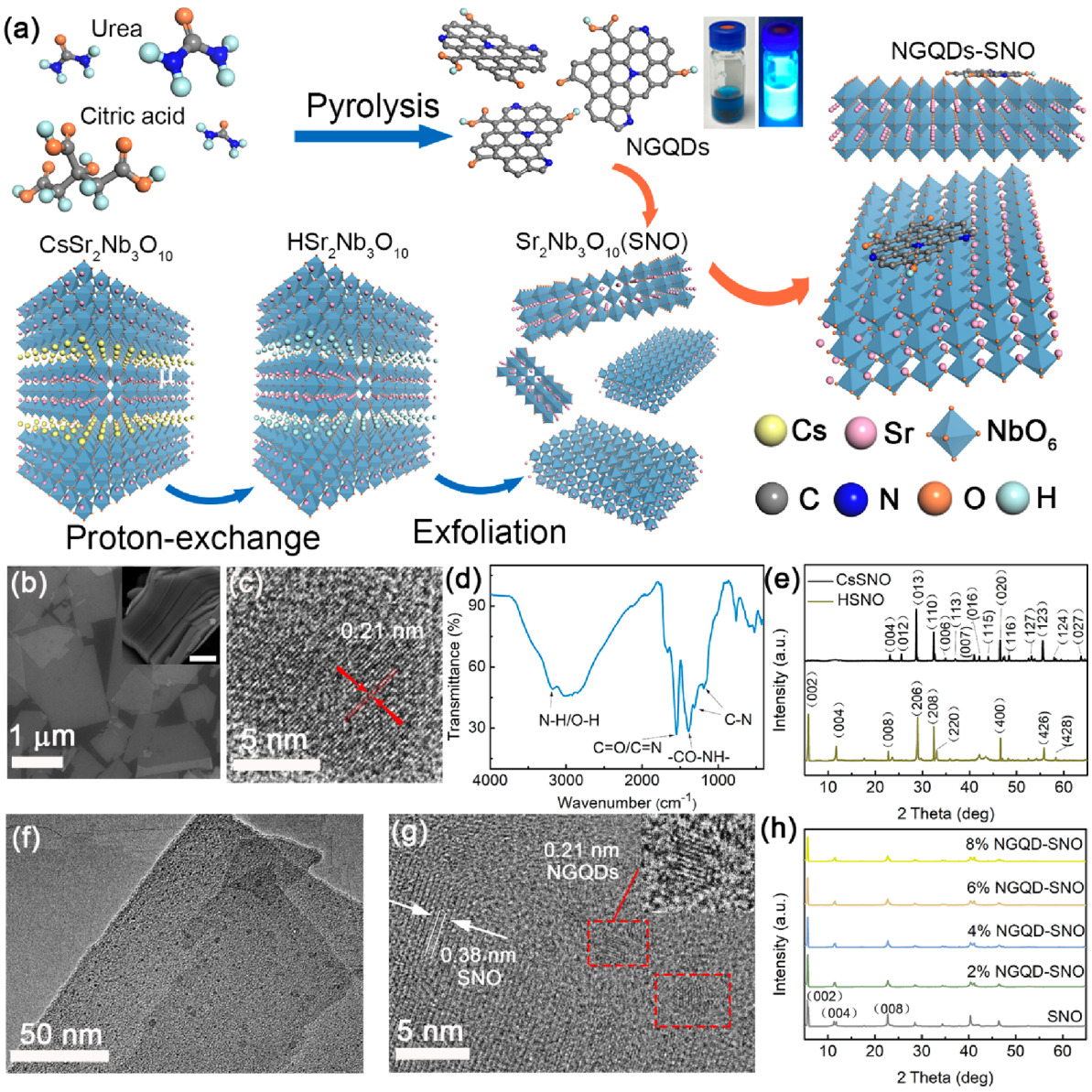

Figure 1. (a) Schematic illustration of the synthesis of the NGQDs-SNO samples. (b) SEM images of the pristine SNO nanosheets; the inset displaying the layered structure of the precursor CsSNO (scale bar: 500 nm). (c) HRTEM image of NGQDs. (d) FTIR spectrum of NGQDs. (e) XRD spectra of the precursor CsSNO and the intermediate product HSNO. (f) TEM image and (g) HRTEM image of the NGQDs-SNO samples. (h) XRD spectra of the pristine SNO nanosheets and NGQDs-SNO samples.

cooled to room temperature and oxidized into a stable green solution in open air. The solution was then mixed with ethanol and centrifuged at 10,000 rpm for 15 min. The precipitated NGQDs were dried in a vacuum at 80 °C for 24 h to obtain the final product. To construct the 0D/2D nanocomposites, the estimated amount of NGQDs was dispersed into the SNO nanosheets suspension with a weight ratio of NGQD/SNO = 2%, 4%, 6%, 8%. The NGQDs were easily dissolved and anchored on the nanosheets without precipitation to form a series of mixed colloids. These colloids were then spin-coated onto glass substrates to obtain the NGQDs-SNO samples.

Characterization of the NGQDs-SNO Samples. A field-emission scanning electron microscopy (FESEM, Zeiss Sigma) and a high-resolution transmission electron microscopy (HRTEM, TECNAI G2 S-TWIN) were utilized to investigate the morphology and microstructures of the samples. X-ray diffraction (XRD) patterns of the samples were obtained from a Bruker D8-A25 diffractometer using Cu Kα radiation (λ = 1.5405 Å). X-ray photoelectron spectroscopy (XPS, PHI 5000C ESCA) was used to characterize the surface elemental composition and the chemical state of the samples. A UV−vis spectrophotometer (Hitachi, U-3900H) was utilized to analyze the optical properties of the samples. The Fourier transform infrared (FTIR) test was carried out on a Thermo Scientific Nicolet iS20 spectrometer.

Photoelectric Measurement. Two pieces of silver pastes with a fixed area and distance were doctoral-bladed onto the composites films as PD electrodes. All the photoelectric behaviors were characterized on a program-controlled semiconductor characterization system (Keithley 4200SCS) under ambient conditions. A 450 W Xe lamp equipped with a monochromator was utilized as the light source, and a NOVA II power meter (OPHIR photonics) was used to measure the incident light density. The pulse response property was tested on a system consisting of a digital oscilloscope (Tektronix DPO 5140B) and a 355 nm Nd:YAG pulsed laser.

Density Functional Theory Calculations. We performed the first-principles calculations in the frame of density functional theory (DFT) with the Vienna ab initio simulation package (VASP). The exchange-correlation energy was described by the Perdew−Burke−Ernzerhof (PBE) form of generalized-gradient approximation (GGA)

https://doi.org/10.1021/acsami.2c15946
ACS Appl. Mater. Interfaces 2022, 14, 48936−48947

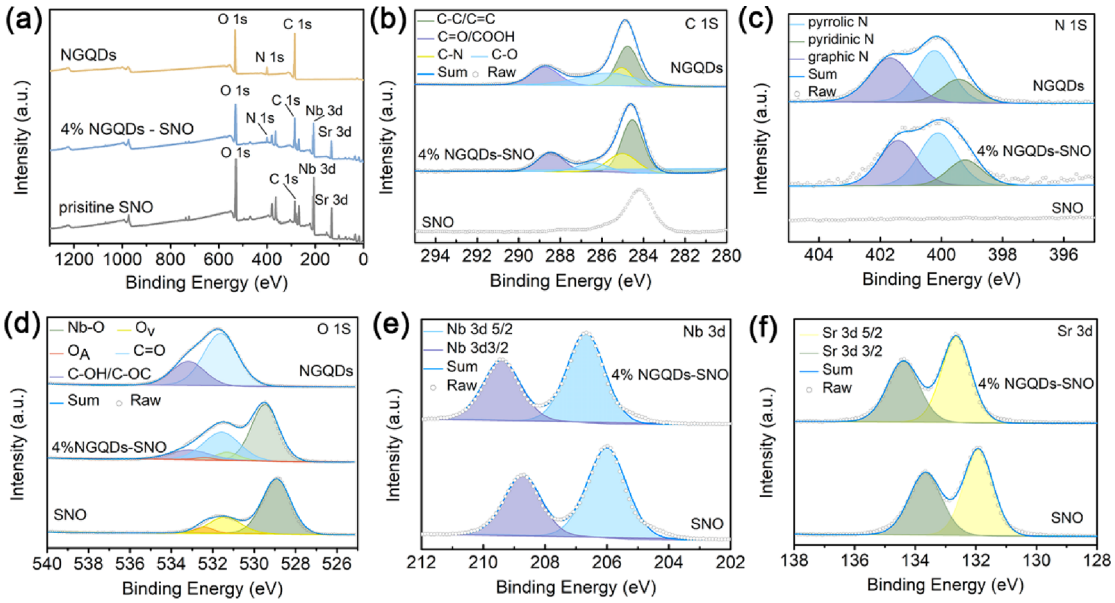

Figure 2. XPS spectra of the pristine SNO, 4%NGQDs-SNO, and NGQDs samples: (a) survey scan, (b) C 1s, (c) N 1s, (d) O 1s, (e) Nb 3d, and (f) Sr 3d spectra.

exchange-correlation energy functional, in combination with the DFT-D3 correction. The structure optimizations were carried out by allowing all atomic positions to vary and fixing lattice parameters until the energy difference of successive atom configurations was less than 10^{-5} eV. The force on each atom in the relaxed structures was less than 0.015 eV/Å. The cutoff energy for the plane-wave basis set was set to 400 eV. The k-point spacing was set to be smaller than 0.03 $Å^{-1}$ over Brillouin zone (BZ). The Hubbard U model was implemented on Nb 3d orbitals to improve the calculated band gap width. The adsorption energy was calculated as $E_{ads} = E(\text{slab} + O_2) - E(\text{slab}) - E(O_2)$, where $E(\text{slab} + O_2)$ and $E(\text{slab})$ represent the total energies of materials with and without adsorbed O_2, respectively. $E(O_2)$ describes the total energy of O_2 molecule in gas phase.

3. RESULTS AND DISCUSSION

Structural and Morphological Characterizations. Figure 1a presents a schematic diagram for fabricating $Sr_2Nb_3O_{10}$ (SNO) nanosheets decorated with nitrogen-doped graphene quantum dots (NGQDs). The nanosheets are prepared through a multistep liquid exfoliation method. The layered precursor $CsSr_2Nb_3O_{10}$ obtained from high-temperature calcination is treated with HCl to replace interlayer Cs^+ ions with protons, and the subsequent exfoliation is conducted by using TBAOH. The 2D morphology of SNO in the SEM image confirms the successful exfoliation (Figure 1b), with the inset showing the layered structure of the precursor. The morphologies of the precursor and the intermediate products are shown in Figure S1. NGQDs are synthesized by a facile hydrothermal method using citric acid and urea. The colloidal NGQD displays a bright blue color under irradiation of a 365 nm UV lamp, which indicates its superior photoluminescence property owing to the carboxylic functional groups and nitrogen doping.[40] The high-resolution transmission electron microscopy (HRTEM) image in Figure 1c confirms the successful synthesis of NGQDs. The interplanar distance of the ordered lattice fringe is calculated to be 0.21 nm, which is derived from the (100) crystal plane of graphite.[47] The structure and composition of the NGQDs are confirmed by the analysis on Fourier transform infrared spectroscopy (FTIR). As shown in Figure 1d, the broad peak centered around 3200 cm^{-1} is assigned to the stretching vibrations of O—H and N—H, the absorption at 1545 cm^{-1} reveals C═N/C═O bonding.[48,49] Furthermore, CO—NH and C—N functional groups could also be identified in the FTIR spectrum.[50,51] NGQDs in a weight ratio of 2%, 4%, 6%, and 8% are facilely mixed with nanosheets dispersed in water solution. The successful attachment of NGQDs on SNO nanosheets can be characterized through transmission electron microscopy. Interestingly, as shown in Figure 1f and Figure S1, NGQDs are uniformly distributed on the surface of SNO nanosheets, exhibiting adsorption affinity toward the SNO surface, while the nitrogen-free graphene quantum dots do not show an adsorption phenomenon. In HRTEM image (Figure 1g), two sets of distinct lattice fringes can be observed. SNO nanosheets exhibit high crystallinity with an interplanar spacing of 0.38 nm (the (100) facet), which is consistent with the XRD results. The other set of ordered lattice fringes with an interplanar spacing of 0.21 nm corresponds to the (100) atomic planes of attached NGQDs. It is supposed that NGQDs have a positively charged surface, which is attributed to the positively charged amino groups as confirmed by the FTIR results.[48,51,52] Thus, NGQDs are spontaneously attached to the negatively charged SNO nanosheets through electrostatic interaction, and a stable hybrid colloid (NGQDs-SNO) is obtained for the subsequent device construction. The X-ray diffraction (XRD) technique is conducted to reveal the crystal structure of the pristine SNO and NGQDs-SNO samples. Figure 1e presents the crystal evolution process; the XRD patterns of the precursor $CsSr_2Nb_3O_{10}$ and the intermediate products $HSr_2Nb_3O_{10}$ both match well with the standard data (PDF#53-1047 and PDF#51-1878, respectively). For the pristine SNO and NGQDs decorated nanosheets, their XRD patterns in Figure 1h exhibit obvious peaks from (00c) planes of SNO, including (002), (004), and (008) planes. The absence of diffraction peaks corresponding to NGQDs might be attributed to the strong intensities of the diffraction peaks from crystalline SNO nanosheets, as well as the high desperation of the small-size NGQDs.[42,43]

https://doi.org/10.1021/acsami.2c15946
ACS Appl. Mater. Interfaces 2022, 14, 48936−48947

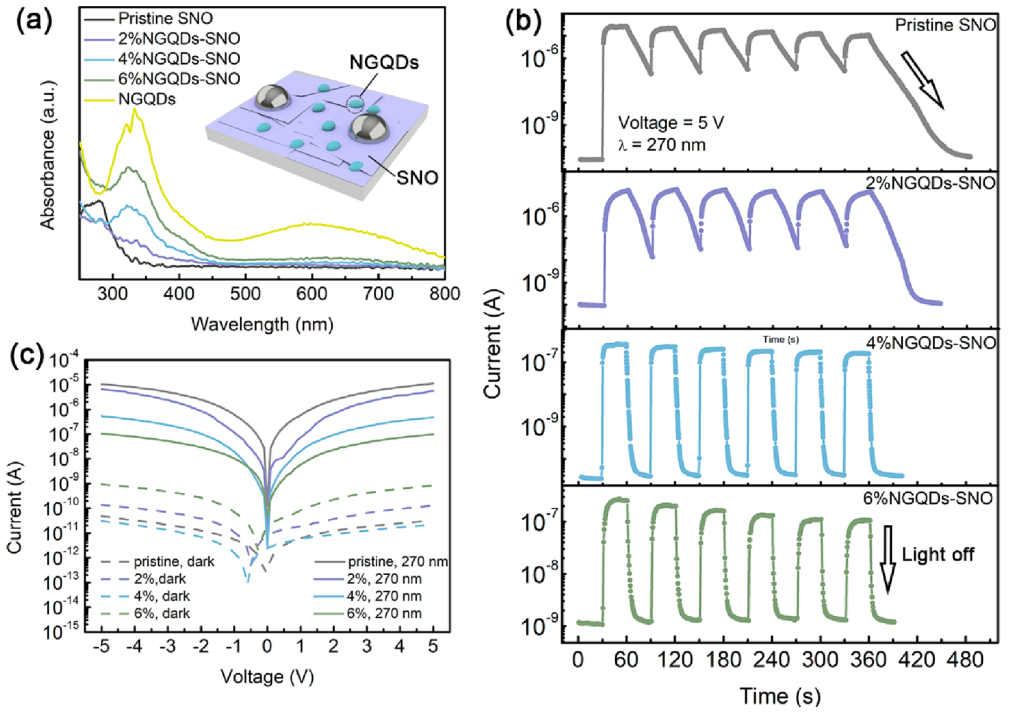

Figure 3. (a) UV−vis absorption spectra of the pristine SNO, NGQDs, and NGQDs-SNO samples. (b) *I*−*t* characteristics of the NGQDs-SNO PDs at 5.0 V bias under 270 nm illumination with a time interval of 30 s. (c) *I*−*V* characteristics of these PDs under dark and 270 nm illumination.

The surface composition and elemental chemical states of the pristine SNO and 4%NGQDs-SNO sample are determined by the X-ray photoelectron spectroscopy (XPS). As shown in Figure 2a, the existence of Sr, Nb, and O elements is confirmed in the 4%NGQDs-SNO sample, and the weak peak of N 1s is indicative of the nitrogen dopants from the NGQDs. High-resolution XPS spectra of C 1s, N 1s, O 1s, Nb 3d, and Sr 3d for the pristine samples and the 4%NGQDs-SNO sample are presented in Figure 2b−f to further reveal the chemical states information. The C 1s spectrum of the NGQDs sample is deconvoluted into four peaks corresponding to C—C/C═C (284.7 eV), C—N (285 eV), C—O (285.7 eV), and C═O/COOH (288.7 eV) bonds. For the 4%NGQDs-SNO sample, the presence of carbon-related bonds mentioned above confirms the formation of the compound structure. The N 1s spectrum of the 4%NGQDs-SNO sample in Figure 2c is mainly resolved into three peaks centered at 399.2, 400.1, and 401.4 eV, which can be assigned to pyridinic N, pyrrolic N, and graphic N, respectively. Figure 2d provides the high-resolution XPS spectra of O 1s in three samples. The O 1s spectrum of the pristine SNO can be deconvoluted into three peaks. In detail, the peak at 528.9 eV is attributed to the lattice oxygen in oxide semiconductors (Nb—O bonds). Notably, two additional peaks appear in the spectrum, with one at 531.4 eV associated with the oxygen vacancies (O_v) and the other one at 532.5 eV arising from the adsorbed oxygen species (O_A) at surface oxygen vacancies or other dangling bonds. The existence of the two peaks is a typical feature of the defect-rich oxides,[53] suggesting that the pristine SNO we prepared contains a certain amount of oxygen-related defects, which would induce the PPC effect and greatly influence the photodetecting performance.[42,54] For the 4%NGQDs-SNO sample, besides the peaks originating from the SNO nanosheets, extra peaks with binding energies of 531.6 and 533.1 eV are observed, which are attributed to C═O and C—OH/C—O—C bonds, respectively. The high-resolution spectra of Nb 3d (Figure 2e) reveal the +5 oxidation state of Nb in the 4% NGQDs-SNO sample, with the Nb 3d 5/2 peak located at 206.6 eV and Nb 3d 3/2 centered at 209.3 eV. Figure 2f displays the spectra of Sr 3d, from which similar peaks can be observed for both samples. The binding energy peaks located at 132.6 and 134.3 eV in the 4%NGQDs-SNO sample are attributed to the spin−orbital splitting photoelectrons of Sr 3d 5/2 and Sr 3d 3/2. Together with TEM images, these XPS results confirm the successful formation of the NGQDs-SNO nanocomposites.

Effect of NGQDs Loading on Photodetecting Performance. To demonstrate the influence of loading different amounts of NGQDs on improving the photodetecting performance of the SNO nanosheets, the PDs are fabricated based on the pristine SNO and the NGQDs-SNO samples. The NGQDs-SNO colloids with various NGQD contents are prepared and spin-coated on the glass substrate. The obtained samples are integrated with Ag pastes to investigate the photodetecting performance. In order to explore whether the incorporation of NGQDs will affect the optical properties of the samples, UV−vis spectroscopy is conducted to compare the absorption properties of the pristine SNO and the NGQDs-SNO samples. As shown in Figure 3a and Figure S2, the absorption edge of the pristine SNO sample locates at 320 nm. The incorporation of the 2%NGQDs broadens the absorption band. When the concentration is further increased, the spectra of 4%, 6%, and 8%NGQDs-SNO samples display two obvious peaks originating from the characteristic absorption peaks of the NGQDs. The peak located below 250 nm corresponds to $\pi-\pi^*$ transition of aromatic C═C domains and the peak centered around 330 nm can be attributed to $n-\pi^*$ transition of C═O or C═N. The absorption spectra exhibit the UV selectivity and an enhanced UV absorption of the NGQDs-SNO composites. Figure 3b,c

https://doi.org/10.1021/acsami.2c15946
ACS Appl. Mater. Interfaces 2022, 14, 48936−48947

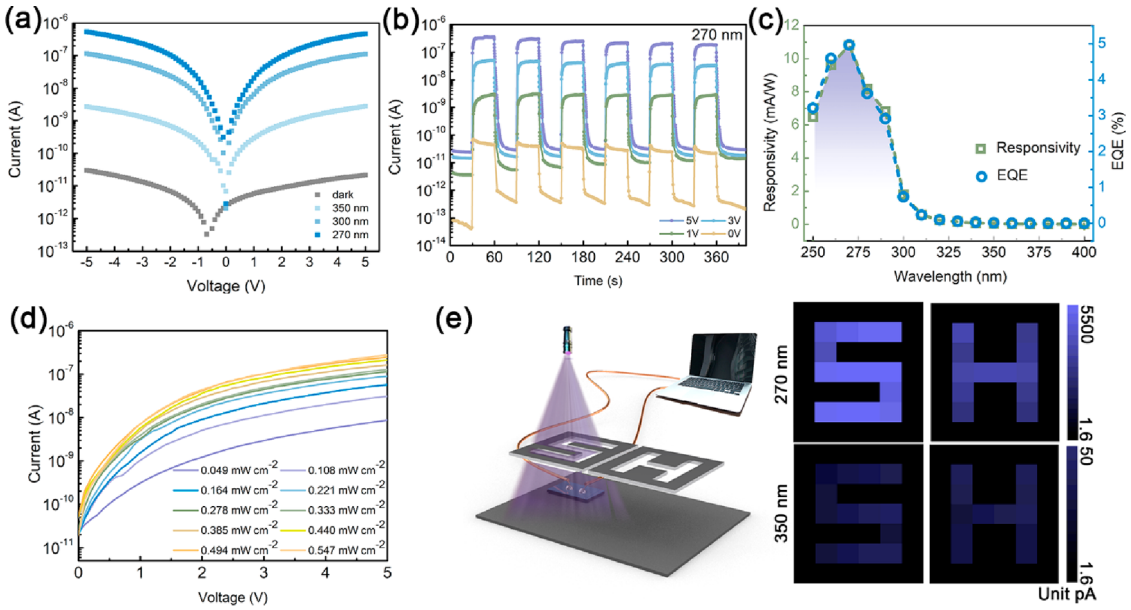

Figure 4. Photodetecting performance of the 4%NGQDs-SNO PD. (a) $I-V$ curves under dark, 350, 300, and 270 nm illumination. (b) $I-t$ curves under 270 nm at 5.0, 3.0, 1.0, and 0 V. (c) Calculated responsivity and EQE curves at 5.0 V bias. (d) $I-V$ curves under 270 nm illumination with various incident light power densities. (e) Schematic illustration of the imaging system for recording UV signal and the image-sensing profile of "SH" under 270 and 350 nm illumination, respectively.

and Figure S2 display the photoelectric properties of the pristine SNO PD and the NGQDs-SNO PDs in dark and under 270 nm UV illumination. In Figure 3b, the time-resolved current ($I-t$) curves are listed to investigate the influence of the NGQDs concentration on the response speed. At a fixed bias of 5.0 V, all the PDs exhibit repeatable cycles in a time interval of 30 s under 270 nm illumination on/off switching. The pristine SNO PD exhibits a very slow decay speed, and the time for the current to recover its original dark state is investigated to be around 120 s, suggesting the long-duration PPC phenomenon. While for the PDs based on the NGQDs-SNO nanocomposite, varying degrees of improvement in the decay speed are observed due to the incremental concentrations of NGQDs. The incorporation of NGQDs endows the 2%NGQD-SNO PD with a slightly faster response speed, and the decay time is reduced to less than 60 s. A increasing loading amount of the NGQDs results in a further reduction in decay time. Obviously, the 4%NGQDS-SNO PD displays complete on/off cycles in the time interval with a rapid decrease in photocurrent after switching off the light, achieving a significantly improved response speed compared to the pristine SNO PD. The decay speed of the PDs is successively improved with the concentration of the NGQDs increased to 6%. Thus, the incorporation of NGQDs effectively improves the response speed of the PDs with the decay time notably shortened from hundreds of seconds to a few seconds. The ultraslow decay of the pristine SNO PD indicates that the lifetime of the photoinduced carriers is prolonged, giving rise to the PPC effect. Note that the recombination process in perovskite oxides is complicated. It is not limited to direct band-to-band recombination of free electrons and holes but significantly influenced by the properties of trap states originating from native defects or foreign adsorbed molecules, which hinders the recovery of the photoconductors after removing the light illumination. The integration of NGQDs and SNO makes a difference in the surface states and the transfer path of photocarriers due to the formed nanoscale heterojunctions, facilitating the recombination process.

However, the photocurrent of the PDs based on NGQDs-SNO samples is unavoidably sacrificed, considering the increased probability of the surface/interface carrier recombination. Figure 3c demonstrates the current−voltage ($I-V$) characteristics of these PDs under dark and 270 nm UV light illumination. The pristine SNO PD at 5.0 V bias yields a photocurrent up to 11.1 μA, which is much higher than that of reported SNO PD. The photocurrent of the 2%NGQDs-SNO PD remains a relatively high value of 5.6 μA. The 4%NGQDs-SNO PD yields a dark current of 21.4 pA and a photocurrent of 0.47 μA, giving a high I_{photo}/I_{dark} ratio of $\approx 2.2 \times 10^4$. The dark current of the PD exhibits a rising trend as the concentration of the NGQDs is increased to 6%−8% (Figure S2), resulting in a decrease in the on−off ratio. A moderate compromise of photocurrent is common and acceptable as reported in other metal oxides like ZnO and Ga_2O_3; since the trapping effect acts as a double-edged sword, the long lifetime of the photocarriers is detrimental to the response speed but conducive to enhanced photoconductive gain.[15,16,55,56] When considering various strategies for solving the problem of slow decay by reducing trap states, it should be taken into account that the reduction in the carrier lifetime inevitably leads to a decrease in the photoconductive gain. Despite this, the photodetecting performance of the 4%NGQDs-SNO PD still remains at a relatively high level.

Performance of the 4%NGQDs-SNO PD and its Application in UV Imaging. The 4%NGQDs-SNO PD exhibits the most outstanding photodetecting performance among all NGQDs-SNO PDs, and the greatly improved decay speed offers it the potential to be applied in image sensing. Figure 4a presents the $I-V$ characteristics of the 4%NGQDs-SNO PD in dark and under 350, 300, and 270 nm illumination. The PD shows a distinct photoresponse toward the incident UV light with the photocurrent reaching its highest value under 270 nm illumination. To further reveal the stability and

https://doi.org/10.1021/acsami.2c15946
ACS Appl. Mater. Interfaces 2022, 14, 48936−48947

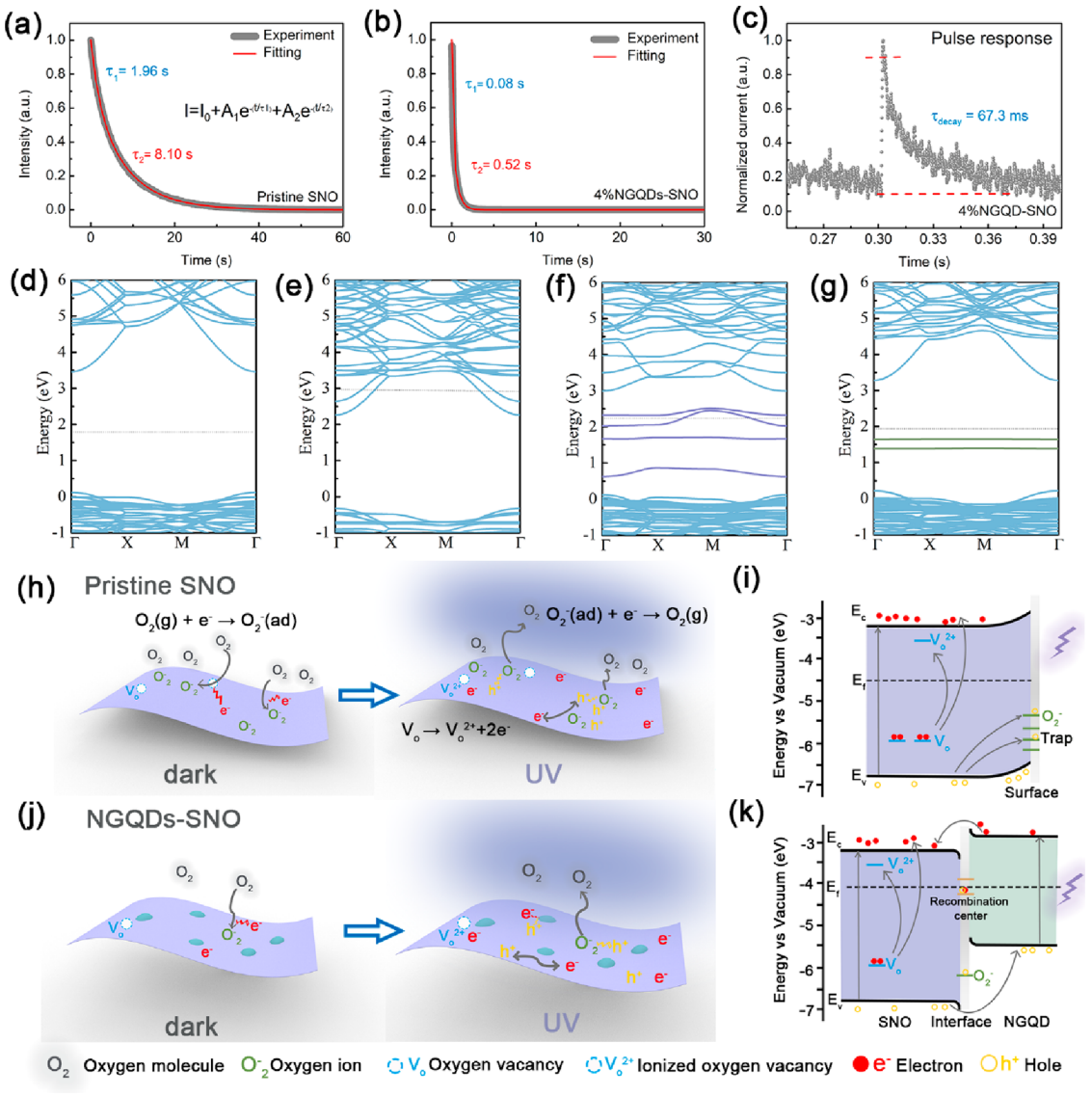

Figure 5. Experimental and fitted curves of the decay process for (a) the pristine SNO PD and (b) the 4%NGQDs-SNO PD. (c) Pulse response curve of the 4%NGQDs-SNO PD. Density functional theory calculations of the electronic structures for (d) defect-free single layer SNO, (e) SNO with two surface V_o, (f) SNO with two inner V_o, and (g) SNO with chemisorbed oxygen molecules on the surface V_o site. Schematic illustration of the carrier transport behavior affected by V_o ionization and O_2 adsorption in the PDs in dark and under UV illumination: (h) the pristine SNO PD and (j) the NGQDs-SNO PD. Schematic energy band diagrams of the PDs under UV illumination: (i) the pristine SNO PD and (k) the NGQDs-SNO PD.

the improved photoresponse speed, the $I-t$ curves with several on−off cycles under various bias voltages of 0−5.0 V are illustrated in Figure 4b. As mentioned above, the 4%NGQDs-SNO PD displays high photodetecting performance with an on−off ratio of over 10^4 at 5.0 V bias. At a bias of 3.0 V, the PD reaches a stable photocurrent of ≈50.7 nA upon UV illumination and rapidly decays to its dark state (16.3 pA) after switching off the light for several repetitions. The PD maintains a high on−off ratio of ≈1.42×10^3 with the voltage bias decreased to 1.0 V. Interestingly, at 0 V bias, the PD exhibits self-powered photodetecting performance with a photocurrent of over 10 pA and an on−off ratio of 1.23×10^2. The self-powered characteristic might be ascribed to the formed electric field introduced by the nanoscale heterojunctions between NGQDs and SNO nanosheets.[28,38]

Spectral photoresponse of the 4%NGQDs-SNO PD is investigated as shown in Figure 4c. The responsivity (R_λ), detectivity (D^*), and external quantum efficiency (EQE) are crucial evaluation parameters, which are defined as follows:

$$R_\lambda = \frac{I_{ph} - I_{dark}}{P_\lambda S} \quad (1)$$

$$D^* = \frac{R_\lambda}{\left(\frac{2eI_{dark}}{S}\right)^{1/2}} \quad (2)$$

$$EQE = \frac{hc}{e}\frac{R_\lambda}{\lambda} \quad (3)$$

where I_{ph} and I_{dark} represent the photocurrent and dark current, S is the effective illumination area, λ is the excitation wavelength, P_λ is the light power density, and h, c, and e are Planck's constant, the light velocity, and the elementary charge, respectively. The 4%NGQDs-SNO PD shows notable photo-

https://doi.org/10.1021/acsami.2c15946
ACS Appl. Mater. Interfaces 2022, 14, 48936−48947

response from 250 to 320 nm with the responsivity peak reaching 10.8 mA W^{-1} under 270 nm illumination at 5.0 V bias, and the corresponding EQE and detectivity are calculated to be 4.97% and 3.39×10^{11} Jones, respectively (Figure 4c and Figure S3). The cutoff wavelength of the 4%NGQDs-SNO PD is consistent with the absorption edge of the pristine SNO, implying that the incorporation of NGQDs has no obvious effect on the spectral selectivity. Figure 4d shows the $I-V$ curves of the PD under 270 nm illumination with various incident light densities. The photogenerated efficiency of charge carriers is positively correlated to the absorbed photon flux. In order to explore the potential of the PD for image sensing, a single-pixel image sensing system is designed based on the 4%NGQDs-SNO PD. As shown in Figure 4e, the UV light beam passes through the hollow masks with S and H patterns (SH = Shanghai), which can be moved continuously along the x-axis and y-axis directions. The position of the masks is recorded in the process of the movement and the corresponding photocurrents that emerged from the PD below the masks are collected synchronously by a Keithley 4200 source meter. The photocurrent mapping images under the illumination of 270 and 350 nm are simulated by arranging the photocurrents according to the position of the mask at each point. The letter "S" and "H" can be distinctively observed in Figure 4e, where the image under 270 nm illumination exhibits a purple pattern and the image under 350 nm illumination shows a relatively lighter one due to the weaker photoresponse. The improved decay speed via incorporation of NGQDs causes the PD to respond instantly to the change of illuminance area. Otherwise, even as the incident light is blocked by the mask, the PD might still maintain a high value of photocurrent due to PPC effect, leading to the blurred boundaries of the letter pattern.

Recovery Dynamics. To unravel the mechanism of the enhanced decay speed, the photocurrent decay process for the pristine SNO and 4%NGQDs-SNO PD are normalized, and the obtained results are presented in Figure 5a,b. The biexponential time constant extraction method is adopted to quantify the recovery dynamics,

$$I_{\text{decay}} = I_0 + A_1 e^{-t/\tau_1} + A_2 e^{-t/\tau_2} \quad (4)$$

where I_0 is the steady-state photocurrent, τ_1 and τ_2 are the relaxation time constants corresponding to two distinct decay processes, and A_1 and A_2 are the weighing factors representing the relative contribution of each mechanism. It is noted that the decay process consists of two components, including a fast decay process (τ_1) and a slow decay process (τ_2). The fast decay is attributed to the band-to-band transition of the photoexcited excess carriers, while the slow decay is related to the detrapping of the photocarriers or other defect-related relaxation process.[9,57] The re-excitation of the trapped carriers and the structural relaxation of the defects require thermal activation, which results in an extra decay time lasting a few seconds or minutes.[5,58] The slow decay photorelaxation time constant τ_2 for the pristine SNO PD is 8.1 s with relative weighing factors of 70%, demonstrating a close dependence of the response speed and the trap states. The decoration of the NGQDs shortens the decay time constant of the NGQDs-SNO PDs to milliseconds. In comparison, both relaxation time constants (τ_1 = 0.08s, τ_2 = 0.52 s) of the 4%NGQDs-SNO PD are much smaller than those of the pristine SNO PD, which implies enhanced carrier recombination and a reduced impact of the trap states, especially the deep traps on the photocarrier transition. Interestingly, when the 4%NGQDs-SNO PD is illuminated with a 355 nm pulse laser instead of continuous light, the photocurrent decays rapidly in 67.3 ms, and the slow decay process associated with PPC is not observed (Figure 5c). A similar phenomenon has been reported in other metal oxides with complex defect distributions.[4,5] The pulse laser with high energy intensity illuminates the sample in an ultrashort time duration; abundant free carriers are generated instantaneously and annihilated rapidly through a band-to-band recombination. However, sufficient illumination is required to activate the potential trap states, such as the ionization of oxygen vacancies and the interaction between photogenerated carriers and adsorbed molecules.[9,58] The disappearance of the slow decay in the pulse speed curve reveals that the trap involved decay process does not emerge during the ultrashort term illumination. Therefore, the photocurrent decay process induced by pulse laser is mainly associated with the band-to-band recombination of the photogenerated excess carriers. In comparison, the large decay time constant τ_2 of the pristine SNO PDs under continuous illumination reliably confirms the dominating role of the trap states in determining the decay speed of the PDs, and the shortened τ_2 in 4%NGQDs-SNO PD indicates a suppressed effect of trap states compared to the pristine SNO PD.

Origin of PPC Effect in the Pristine SNO PD. As revealed by XPS data (Figure 2d), the SNO nanosheet contains a high density of oxygen vacancies (V_o) and adsorbed oxygen molecules, which might induce trap states. To elucidate the origin of the PPC effect in the pristine SNO, the impact of V_o and adsorbed oxygen molecules on electronic band structure is investigated using DFT calculations (Figure 5d–g and Figures S4–S6). A 2 × 2 supercell slab of defect-free SNO is constructed, and its defective models are built by removing one or two oxygen atoms from the slab surface or volume, considering the various V_o distributions, as shown in Figure S4. Figure 5d presents the band structure of a defect-free SNO slab. The calculated bandgap width is 3.34 eV, which is slightly narrower than the experimental bandgap. As shown in the electronic band structure of the SNO with one and two surface V_o (Figure 5e and Figure S5a), the introduction of V_o at the surface raises the Fermi level and narrows the bandgap, achieving the n-doping of the clear SNO. Two surface oxygen vacancies raise the Fermi level above the conduction band minimum and V_o can act as shallow donors to donate free electrons to the conduction band. Therefore, in addition to the photogenerated electrons through interband transition, the electrons generated by shallow V_o donor can contribute to the high photocurrent.[4]Figure 5f and Figure S5b reveal that the inner V_o results in a narrowed bandgap and the formation of several defect levels. Apparently, two inner V_o introduce several defect levels within the bandgap, with their positions far from the valence band or the conduction band. The deep, neutral V_o states located in the bandgap can be ionized to shallow donor states V_o^{2+} and release two electrons to the conduction band. An energy barrier needs to be overcome due to the outward relaxation of bonds surrounding the V_o sites, thus resulting in the persistent high photoconductivity.[10] In addition to the trap states introduced by the lattice defects, the impact of adsorbed oxygen molecules cannot be ignored (Figure 5g and Figure S6). It is known that the surface V_o or other dangling bonds are more preferable adsorption sites for oxygen molecules than the defect-free sites.[32] Here, the O_2 adsorption process is

https://doi.org/10.1021/acsami.2c15946
ACS Appl. Mater. Interfaces 2022, 14, 48936−48947

simulated by inserting an O_2 molecular into the surface V_o, and the adsorption energy is calculated to be −0.64 eV (Figure S6a). The electronic band structure and total density of states (DOS) are plotted in Figure 5g and Figure S6b. Obviously, the adsorption of O_2 induces deep trap states within the bandgap, which might prolong the lifetime of the photocarriers, resulting in the high photoconductive gain and extra decay time required for carrier detrapping.

Carrier-Transport Behavior in the Pristine SNO and NGQDs-SNO PD. According to the results of the calculation, the schematic diagrams of the transport behavior of the photocarriers are plotted in Figure 5h−k to further reveal the mechanism of the PPC phenomenon in the pristine SNO PD and the surface/interface carrier-transport modulation in the NGQDs-SNO PDs. For the pristine SNO PD (Figure 5h,i), in dark conditions, the V_o might exist both on the surface and inside the nanosheet in the synthesis process due to the complex solid-state reaction and destructive exfoliation process. Even if the oxygen is removed, the two oxygen-bond electrons remain in the oxide and generally introduce defect states into the wide bandgap in metal oxide. On the other hand, oxygen molecules are chemisorbed onto the surface by capturing the free carriers in the n-type SNO ($O_{2(g)} + e^- \rightarrow O_2^-{}_{(ad)}$), which leads to a negative charge distribution at the surface and thus gives rise to an upward band bending (Figure 5i). A certain amount of surface trap states would be formed as a result of the interaction between the nanosheet surface and oxygen molecules.[14] Under UV illumination, both O_2^- and V_o in SNO are involved in interfering the photocarrier dynamics (Figure 5i). Electron−hole pairs are generated ($h\nu \rightarrow e^- + h^+$), holes tend to accumulate at the nanosheet surface due to the bult-in potential produced by the band bending, and thereby the electron and holes are spatially separated. The desorption of the oxygen molecules occurs, since the holes captured by the surface trap states neutralize the negatively charged oxygen molecules ($O_2^-{}_{(ad)} + h^+ \rightarrow O_{2(g)}$), leaving behind the long-lived electrons, which contributes to high photoconductivity and slow recombination rate.[28] Simultaneously, the illumination might ionize the deep, neutral V_o states to shallow donor states V_o^{2+} by donating electrons to the conduction band ($V_o \rightarrow V_o^{2+} + 2e^-$), and the emission of the excess electrons increases the electron doping concentration and raises the Fermi level, resulting in the enhanced photoconductivity. The neutralization of the metastable V_o^{2+} states requires overcoming an energy barrier to achieve the relaxation of bonds surrounding V_o and, simultaneously, electrons must be captured from the conduction band; thus, the material maintains a high conductivity after switching off the light.[59] It has been established that the decay process caused by the annihilation of metastable donors or detrapping of the carriers requires thermal activation,[58,60] which can be described as

$$\tau = \tau_0 \exp\left(-\frac{E_a}{KT}\right) \quad (5)$$

where E_a is the thermal activation energy. Therefore, trapping of the holes, coupled with the ionization of the oxygen vacancies requires extra relaxation time, giving rise to the PPC effect.

The decoration of the NGQDs on SNO nanosheets incorporates nanoscale heterojunctions,[28] effectively improving the decay speed of the PD with both time constants greatly reduced. The contact between the NGQDs and SNO nanosheets modulates the surface/interface states. As shown in Figure 5j,k, in dark conditions, the existence of the quantum dots reduces the exposed area of the SNO, hindering the interaction between the nanosheets and oxygen molecules. Fewer oxygen molecules would be adsorbed onto the surface and the upward band bending is weakened. Besides, from the point of band alignment, the experimental bandgap of the SNO is estimated to be around 3.6 eV by the Tauc plot and the valence band position and the work function are determined by KPFM and XPS results in Figure S7. The bandgap and the electron affinity of NGQDs are approximately 2.6 and 2.9 eV, respectively, according to the previous reports.[42,61] Thus, a type II heterojunction can be formed between SNO and NGQDs (Figure 5k). Excess electrons in NGQDs transfer to SNO, which contributes to an internal electric field at the interface between them. The downward band bending of the SNO is opposite to the upward band bending caused by the adsorption of oxygen molecules. In addition, NGQDs with abundant oxygen-rich functional groups have a possibility to interact with the SNO surface oxygen vacancies, and to some extent, it will affect the trap states originating from the oxygen vacancies.[62] Nevertheless, the decoration of the NGQDs would have no effect on the deep localized V_o states inside the nanosheet. Under UV light illumination, the photogenerated carriers are generated in the NGQDs-SNO PD. Due to the formation of the interface between NGQDs and SNO, the surface oxygen adsorption is reduced and the change of the band bending direction hinders the accumulation of the photogenerated holes at the surface. Thus, fewer photoinduced holes are trapped to neutralize the negatively charged O_2^-, and the extra time required to empty traps is reduced (Figure 5j). On the other hand, the built-in electric field caused by heterojunction would play a role in guiding the photocarriers behavior. The electrons transfer from NGQDs to SNO, and the holes are driven to NGQDs (Figure 5k). When the UV light is switched off, the electron−hole recombination takes place though the direct band-to-band recombination in both SNO and NGQDs, and the high carrier mobility in NGQDs facilitates direct recombination, Therefore, the decay time constants τ_1 and τ_2 are both reduced due to the coeffect of the reduced trap states and the built-in field of the NGQDs-SNO heterojunction. However, the extra decay time due to the ionization of the oxygen vacancies remains an unsolved problem, which can explain the main difference between the decay time under continuous and pulse illumination (Figure 5b,c).

Despite the improved decay speed, a decrease of the photocurrent is unavoidable in the NGQDs-SNO PDs considering the relationship between the carrier lifetime and the photoconductive gain. As mentioned above, the trap states contribute to the long-lived electrons ad enhance the photoconductive gain according to the formula.[63]

$$G = \frac{\tau_c}{\tau_t} \quad (6)$$

where τ_c is the carrier lifetime and τ_t is the carrier transit time. The decoration of the NGQDs hinders the effect of the trap states; thus, the lifetime of the photocarriers is reduced and the photoresponse is limited. Moreover, the lattice mismatch between SNO and NGQDs would bring about recombination centers, i.e., a type of localized states that can facilitate the recombination of electrons and holes. Whether the localized

https://doi.org/10.1021/acsami.2c15946
ACS Appl. Mater. Interfaces 2022, 14, 48936−48947

states act as recombination centers or trap states depends on their relative positions to the quasi- Fermi levels. The states between the quasi-Fermi levels act as recombination centers, while the states above/below the electron/hole quasi-Fermi levels are the trap states for electrons and holes, respectively.[5,38] Thus, in contrast to surface trap states induced by adsorbed O_2, the localized states at the interface might act as recombination centers, which is detrimental to the photocurrent but facilitates the recombination process.

4. CONCLUSIONS

In summary, by integrating NGQDs and 2D perovskite oxide SNO nanosheets through electrostatic interaction, a novel nanoscale heterojunction is designed to tackle the problem of slow response speed of pristine SNO PDs. The slow response speed is attributed to the PPC effect due to the existence of abundant oxygen-related defects in SNO. NGQDs-SNO nanocomposites with various NGQD contents are designed to alter the surface states of SNO nanosheets and thereby modulate the surface/interface carrier transport. In compared with the pristine SNO PD, The NGQDs-SNO PDs show greatly enhanced response speed with the decay time shortened from hundreds of seconds to within seconds. The 4%NGQD-SNO PD exhibits excellent photodetecting performance with a photocurrent of 0.47 μA, a high on−off ratio of 2.2×10^4, and a fast pulse response speed (τ_{decay} = 67.3 ms), making it promising for the application of UV image sensors. The analysis of relaxation dynamics reveals that, instead of the direct band-to-band recombination, the trap-involved decay process plays a dominant role in determining the decay time, which results in the PPC effect in SNO. Meanwhile, the DFT results confirm that the oxygen vacancies and the adsorbed oxygen molecules would bring about trap states in the material electronic structure. The integration of NGQDs on SNO nanosheet reduces surface trap states and minimizes the interaction between the photocarriers and the chemisorbed oxygen molecules. In addition, the formed nanoscale heterojunction provides an efficient carrier pathway for facilitating the recombination of free carriers after the light source is turned off. This work provides an effective way for the enhancement of the response speed in 2D perovskite oxides constrained by the PPC effect via surface/interface carrier transport modulation.

ASSOCIATED CONTENT

Supporting Information

The Supporting Information is available free of charge at https://pubs.acs.org/doi/10.1021/acsami.2c15946.

Figures of SEM and TEM images, UV−vis absorption spectrum, $I-V$ and $I-t$ characteristics, detectivity curve of the 4%NGQDs-SNO PD as a function of wavelength, corresponding fitting curve for the relationship between the photocurrent values of the 4%NGQDs-SNO PD and the light intensities of 270 nm UV light illumination, optimized structures, density functional theory calculations, analysis of the absorption structure, total DOS diagram, Tauc curve corresponding to the absorption curve of SNO, XPS valance spectrum of SNO, and AFM image and KPFM image of SNO (PDF)

AUTHOR INFORMATION

Corresponding Author

Xiaosheng Fang − *Department of Materials Science, State Key Laboratory of Molecular Engineering of Polymers, Fudan University, Shanghai 200433, P. R. China;* orcid.org/0000-0003-3387-4532; Email: xshfang@fudan.edu.cn

Authors

Xinya Liu − *Department of Materials Science, State Key Laboratory of Molecular Engineering of Polymers, Fudan University, Shanghai 200433, P. R. China*

Siyuan Li − *Department of Chemistry, City University of Hong Kong, Hong Kong 999077, P. R. China*

Ziqing Li − *Institute of Optoelectronics, Fudan University, Shanghai 200433, P. R. China;* orcid.org/0000-0002-8126-2728

Fa Cao − *Department of Materials Science, State Key Laboratory of Molecular Engineering of Polymers, Fudan University, Shanghai 200433, P. R. China*

Li Su − *Department of Materials Science, State Key Laboratory of Molecular Engineering of Polymers, Fudan University, Shanghai 200433, P. R. China*

Dmitry V. Shtansky − *National University of Science and Technology "MISIS", Moscow 119049, Russia;* orcid.org/0000-0001-7304-2461

Complete contact information is available at: https://pubs.acs.org/10.1021/acsami.2c15946

Notes

The authors declare no competing financial interest.

ACKNOWLEDGMENTS

This work was supported by National Natural Science Foundation of China (No. 12061131009 and 51872050) and Science and Technology Commission of Shanghai Municipality (No. 21520712600 and 19520744300). D.V.S. thanks the financial support from the Russian Science Foundation (No. 21-49-00039).

REFERENCES

(1) Ouyang, W.; Teng, F.; He, J.-H.; Fang, X. S. Enhancing the Photoelectric Performance of Photodetectors Based on Metal Oxide Semiconductors by Charge-Carrier Engineering. *Adv. Funct. Mater.* **2019**, *29*, 1807672.

(2) Kublitski, J.; Hofacker, A.; Boroujeni, B. K.; Benduhn, J.; Nikolis, V. C.; Kaiser, C.; Spoltore, D.; Kleemann, H.; Fischer, A.; Ellinger, F.; et al. Reverse Dark Current in Organic Photodetectors and the Major Role of Traps as Source of Noise. *Nat. Commun.* **2021**, *12*, 551.

(3) Doherty, T. A. S.; Winchester, A. J.; Macpherson, S.; Johnstone, D. N.; Pareek, V.; Tennyson, E. M.; Kosar, S.; Kosasih, F. U.; Anaya, M.; Abdi-Jalebi, M.; et al. Performance-Limiting Nanoscale Trap Clusters at Grain Junctions in Halide Perovskites. *Nature* **2020**, *580*, 360−366.

(4) Lee, Y.; Yoon, D.; Yu, S.; Sim, H.; Park, Y.; Nam, Y.-S.; Kim, K.-J.; Choi, S.-Y.; Kang, Y.; Son, J. Reversible Manipulation of Photoconductivity Caused by Surface Oxygen Vacancies in Perovskite Stannates with Ultraviolet Light. *Adv. Mater.* **2022**, *34*, 2107650.

(5) Jiang, J.; Ling, C.; Xu, T.; Wang, W.; Niu, X.; Zafar, A.; Yan, Z.; Wang, X.; You, Y.; Sun, L.; et al. Defect Engineering for Modulating the Trap States in 2D Photoconductors. *Adv. Mater.* **2018**, *30*, 1804332.

(6) Cao, F.; Jin, L.; Wu, Y.; Ji, X. High-performance, Self-powered UV Photodetector Based on Au Nanoparticles Decorated ZnO/CuI Heterostructure. *J. Alloys Compd.* **2021**, *859*, 158383.

(7) Chen, Y. H.; Su, L. X.; Jiang, M. M.; Fang, X. S. Switch Type PANI/ZnO Core-shell Microwire Heterojunction for UV Photodetection. *J. Mater. Sci. Technol.* **2022**, *105*, 259.
(8) Yoo, H.; Lee, I. S.; Jung, S.; Rho, S. M.; Kang, B. H.; Kim, H. J. A Review of Phototransistors Using Metal Oxide Semiconductors: Research Progress and Future Directions. *Adv. Mater.* **2021**, *33*, 2006091.
(9) Wang, C.; Lu, W.; Li, F.; Ning, H.; Ma, F. Persistent Photoconductivity in a-IGZO Thin Films Induced by Trapped Electrons and Metastable Donors. *J. Appl. Phys.* **2022**, *131*, 125709.
(10) Jeon, S.; Ahn, S.-E.; Song, I.; Kim, C. J.; Chung, U. I.; Lee, E.; Yoo, I.; Nathan, A.; Lee, S.; Ghaffarzadeh, K.; et al. Gated Three-terminal Device Architecture to Eliminate Persistent Photoconductivity in Oxide Semiconductor Photosensor Arrays. *Nat. Mater.* **2012**, *11*, 301−305.
(11) Hu, W. J.; Paudel, T. R.; Lopatin, S.; Wang, Z.; Ma, H.; Wu, K.; Bera, A.; Yuan, G.; Gruverman, A.; Tsymbal, E. Y.; et al. Colossal X-Ray-Induced Persistent Photoconductivity in Current-Perpendicular-to-Plane Ferroelectric/Semiconductor Junctions. *Adv. Funct. Mater.* **2018**, *28*, 1704337.
(12) Ouyang, W.; Chen, J. X.; Shi, Z. F.; Fang, X. S. Self-powered UV Photodetectors Based on ZnO Nanomaterials. *Appl. Phys. Rev.* **2021**, *8*, 031315.
(13) Prades, J. D.; Hernandez-Ramirez, F.; Jimenez-Diaz, R.; Manzanares, M.; Andreu, T.; Cirera, A.; Romano-Rodriguez, A.; Morante, J. R. The Effects of Electron-Hole Separation on the Photoconductivity of Individual Metal Oxide Nanowires. *Nanotechnology* **2008**, *19*, 465501.
(14) Teng, F.; Zheng, L. X.; Hu, K.; Chen, H. Y.; Li, Y. M.; Zhang, Z. M.; Fang, X. S. A Surface Oxide Thin Layer of Copper Nanowires Enhanced UV Selective Response of ZnO Film Photodetector. *J. Mater. Chem. C* **2016**, *4*, 8416.
(15) Yang, F.; Guo, J.; Zhao, L.; Shang, W.; Gao, Y.; Zhang, S.; Gu, G.; Zhang, B.; Cui, P.; Cheng, G.; et al. Tuning Oxygen Vacancies and Improving UV Sensing of ZnO Nanowire by Micro-Plasma Powered by a Triboelectric Nanogenerator. *Nano Energy* **2020**, *67*, 104210.
(16) Qian, L. X.; Gu, Z. W.; Huang, X. D.; Liu, H. Y.; Lv, Y. J.; Feng, Z. H.; Zhang, W. L. Comprehensively Improved Performance of beta-Ga_2O_3 Solar-Blind Photodetector Enabled by a Homojunction with Unique Passivation Mechanisms. *ACS Appl. Mater. Interfaces* **2021**, *13*, 40837−40846.
(17) Pan, X.; Ding, L. Application of Metal Halide Perovskite Photodetectors. *J. Semiconductors* **2022**, *43*, 020203.
(18) Gu, L.; Poddar, S.; Lin, Y.; Long, Z.; Zhang, D.; Zhang, Q.; Shu, L.; Qiu, X.; Kam, M.; Javey, A.; et al. A Biomimetic Eye with a Hemispherical Perovskite Nanowire Array Retina. *Nature* **2020**, *581*, 278−282.
(19) Li, Z.; Hong, E.; Zhang, X.; Deng, M.; Fang, X. S. Perovskite-Type 2D Materials for High-Performance Photodetectors. *J. Phys. Chem. Lett.* **2022**, *13*, 1215−1225.
(20) Cao, F.; Yan, T.; Li, Z.; Wu, L.; Fang, X. S. Dual-Band Perovskite Bulk Heterojunction Self-Powered Photodetector for Encrypted Communication and Imaging. *Adv. Opt. Mater.* **2022**, *10*, 2200786.
(21) Li, S.; Zhang, Y.; Yang, W.; Liu, H.; Fang, X. S. 2D Perovskite $Sr_2Nb_3O_{10}$ for High-Performance UV Photodetectors. *Adv. Mater.* **2020**, *32*, 1905443.
(22) Warren, W. L.; Vanheusden, K.; Dimos, D.; Pike, G. E.; Tuttle, B. A. Oxygen Vacancy Motion in Perovskite Oxides. *J. Am. Ceram. Soc.* **1996**, *79*, 536−538.
(23) Ji, Q.; Bi, L.; Zhang, J.; Cao, H.; Zhao, X. S. The Role of Oxygen Vacancies of ABO_3 Perovskite Oxides in the Oxygen Reduction Reaction. *Energy Environ. Sci.* **2020**, *13*, 1408−1428.
(24) Tan, H.; Zhao, Z.; Zhu, W. B.; Coker, E. N.; Li, B.; Zheng, M.; Yu, W.; Fan, H.; Sun, Z. Oxygen Vacancy Enhanced Photocatalytic Activity of Pervoskite $SrTiO_3$. *ACS Appl. Mater. Interfaces* **2014**, *6*, 19184.
(25) Gunkel, F.; Christensen, D. V.; Chen, Y. Z.; Pryds, N. Oxygen Vacancies: The (in)visible Friend of Oxide Electronics. *Appl. Phys. Lett.* **2020**, *116*, 120505.
(26) Zu, X.; Zhao, Y.; Li, X.; Chen, R.; Shao, W.; Wang, Z.; Hu, J.; Zhu, J.; Pan, Y.; Sun, Y.; et al. Ultrastable and Efficient Visible-light-driven CO_2 Reduction Triggered by Regenerative Oxygen-Vacancies in $Bi_2O_2CO_3$ Nanosheets. *Angew. Chem., Int. Ed.* **2021**, *60*, 13840−13846.
(27) Zeng, P.; Wang, W.; Jiang, J.; Liu, Z.; Han, D.; Hu, S.; He, J.; Zheng, P.; Zheng, H.; Zheng, L.; et al. Thickness-Dependent Enhanced Optoelectronic Performance of Surface Charge Transfer-Doped ReS_2 Photodetectors. *Nano Res.* **2022**, *15*, 3638−3646.
(28) Retamal, J. R. D.; Chen, C.-Y.; Lien, D.-H.; Huang, M. R. S.; Lin, C.-A.; Liu, C.-P.; He, J.-H. Concurrent Improvement in Photogain and Speed of a Metal Oxide Nanowire Photodetector through Enhancing Surface Band Bending via Incorporating a Nanoscale Heterojunction. *ACS Photonics* **2014**, *1*, 354−359.
(29) Sakthivel, R.; He, J. H.; Chung, R. J. Self-Templating Hydrothermal Synthesis of Carbon-Confined Double-Shelled Ni/NiO Hollow Microspheres for Diphenylamine Detection in Fruit Samples. *J. Hazard. Mater.* **2022**, *424*, 127378.
(30) Le, V.-Q.; Do, T.-H.; Retamal, J. R. D.; Shao, P.-W.; Lai, Y.-H.; Wu, W.-W.; He, J.-H.; Chueh, Y.-L.; Chu, Y.-H. Van der Waals Heteroepitaxial AZO/NiO/AZO/Muscovite (ANA/Muscovite) Transparent Flexible Memristor. *Nano Energy* **2019**, *56*, 322−329.
(31) Yang, W.; Hu, K.; Teng, F.; Weng, J.; Zhang, Y.; Fang, X. S. High-Performance Silicon-Compatible Large-Area UV-to-Visible Broadband Photodetector Based on Integrated Lattice-Matched Type II Se/n-Si Heterojunctions. *Nano Lett.* **2018**, *18*, 4697−4703.
(32) Ding, M.; Guo, Z.; Chen, X.; Ma, X.; Zhou, L. Surface/Interface Engineering for Constructing Advanced Nanostructured Photodetectors with Improved Performance: A Brief Review. *Nanomaterials* **2020**, *10*, 362.
(33) Fu, H. C.; Ramalingam, V.; Kim, H.; Lin, C. H.; Fang, X. S.; Alshareef, H. N.; He, J. H. MXene-Contacted Silicon Solar Cells with 11.5% Efficiency. *Adv. Energy Mater.* **2019**, *9*, 1900180.
(34) Yang, W.; Chen, J.; Zhang, Y.; Zhang, Y.; He, J. H.; Fang, X. S. Silicon-Compatible Photodetectors: Trends to Monolithically Integrate Photosensors with Chip Technology. *Adv. Funct. Mater.* **2019**, *29*, 1808182.
(35) Xu, F.; Meng, K.; Cheng, B.; Wang, S.; Xu, J.; Yu, J. Unique S-scheme Heterojunctions in Self-Assembled TiO_2/$CsPbBr_3$ Hybrids for CO_2 Photoreduction. *Nat. Commun.* **2020**, *11*, 4613.
(36) Yan, Y.; Zhai, D.; Liu, Y.; Gong, J.; Chen, J.; Zan, P.; Zeng, Z.; Li, S.; Huang, W.; Chen, P. van der Waals Heterojunction between a Bottom-Up Grown Doped Graphene Quantum Dot and Graphene for Photoelectrochemical Water Splitting. *ACS Nano* **2020**, *14*, 1185−1195.
(37) Sreeshma, D.; Janani, B.; Jagtap, A.; Abhale, A.; Rao, K. Defect Studies on Short-Wave Infrared Photovoltaic Devices Based on HgTe Nanocrystals/TiO_2 Heterojunction. *Nanotechnology* **2020**, *31*, 385701.
(38) Zheng, Z.; Gan, L.; Zhang, J.; Zhuge, F.; Zhai, T. An Enhanced UV-Vis-NIR and Flexible Photodetector Based on Electrospun ZnO Nanowire Array/PbS Quantum Dots Film Heterostructure. *Adv. Sci.* **2017**, *4*, 1600316.
(39) Li, H.-J.; Sun, X.; Xue, F.; Ou, N.; Sun, B.-W.; Qian, D.-J.; Chen, M.; Wang, D.; Yang, J.; Wang, X. Redox Induced Fluorescence On-Off Switching Based on Nitrogen Enriched Graphene Quantum Dots for Formaldehyde Detection and Bioimaging. *ACS Sustainable Chem. Eng.* **2018**, *6*, 1708−1716.
(40) Ganganboina, A. B.; Chowdhury, A. D.; Doong, R.-A. N-Doped Graphene Quantum Dots-Decorated V_2O_5 Nanosheet for Fluorescence Turn Off-On Detection of Cysteine. *ACS Appl. Mater. Interfaces* **2018**, *10*, 614−624.
(41) Tetsuka, H.; Nagoya, A.; Fukusumi, T.; Matsui, T. Molecularly Designed, Nitrogen-Functionalized Graphene Quantum Dots for Optoelectronic Devices. *Adv. Mater.* **2016**, *28*, 4632−4638.

https://doi.org/10.1021/acsami.2c15946
ACS Appl. Mater. Interfaces 2022, 14, 48936−48947

(42) Murali, G.; Reddeppa, M.; Seshendra Reddy, C.; Park, S.; Chandrakalavathi, T.; Kim, M. D.; In, I. Enhancing the Charge Carrier Separation and Transport via Nitrogen-Doped Graphene Quantum Dot-TiO_2 Nanoplate Hybrid Structure for an Efficient NO Gas Sensor. *ACS Appl. Mater. Interfaces* **2020**, *12*, 13428−13436.
(43) Chang, W.; Ning, B.; Xu, Q.; Jiang, H.; Hu, Y.; Li, C. Strongly Coupled N-doped Graphene Quantum Dots/Ni(Fe)O_xH_y Electrocatalysts with Accelerated Reaction Kinetics for Water Oxidation. *Chem. Eng. J.* **2022**, *430*, 133068.
(44) Li, B.; Lai, C.; Zhang, M.; Liu, S.; Yi, H.; Liu, X.; An, N.; Zhou, X.; Li, L.; Fu, Y.; et al. N, S-GQDs and Au Nanoparticles Co-modified Ultrathin Bi_2MoO_6 Nanosheet with Enhanced Charge Transport Dynamics for Full-Spectrum-Light-Driven Molecular Oxygen Activation. *Chem. Eng. J.* **2021**, *409*, 128281.
(45) Sun, X.; Li, H. J.; Ou, N.; Lyu, B.; Gui, B.; Tian, S.; Qian, D.; Wang, X.; Yang, J. Visible-Light Driven TiO_2 Photocatalyst Coated with Graphene Quantum Dots of Tunable Nitrogen Doping. *Molecules* **2019**, *24*, 344.
(46) Kong, D.; Wang, Y.; Huang, S.; Lim, Y. V.; Zhang, J.; Sun, L.; Liu, B.; Chen, T.; Valdivia y Alvarado, P.; Yang, H. Y. Surface Modification of $Na_2Ti_3O_7$ Nanofibre Arrays Using N-doped Graphene Quantum Dots as Advanced Anodes for Sodium-ion Batteries with Ultra-stable and High-Rate Capability. *J. Mater. Chem. A* **2019**, *7*, 12751−12762.
(47) Chen, Z.; Mou, K.; Wang, X.; Liu, L. Nitrogen-Doped Graphene Quantum Dots Enhance the Activity of Bi_2O_3 Nanosheets for Electrochemical Reduction of CO_2 in a Wide Negative Potential Region. *Angew. Chem., Int. Ed.* **2018**, *57*, 12790−12794.
(48) Wang, L.; Wu, B.; Li, W.; Wang, S.; Li, Z.; Li, M.; Pan, D.; Wu, M. Amphiphilic Graphene Quantum Dots as Self-Targeted Fluorescence Probes for Cell Nucleus Imaging. *Adv. Biosyst.* **2018**, *2*, 1700191.
(49) Arcudi, F.; Dordevic, L.; Prato, M. Synthesis, Separation, and Characterization of Small and Highly Fluorescent Nitrogen-Doped Carbon NanoDots. *Angew. Chem., Int. Ed.* **2016**, *55*, 2107−2112.
(50) Riaz, R.; Ali, M.; Anwer, H.; Ko, M. J.; Jeong, S. H. Highly Porous Self-Assembly of Nitrogen-doped Graphene Quantum Dots over Reduced Graphene Sheets for Photo-Electrocatalytic Electrode. *J. Colloid Interface Sci.* **2019**, *557*, 174−184.
(51) Li, F.; Cai, Q.; Hao, X.; Zhao, C.; Huang, Z.; Zheng, Y.; Lin, X.; Weng, S. Insight into the DNA Adsorption on Nitrogen-doped Positive Carbon Dots. *RSC Adv.* **2019**, *9*, 12462−12469.
(52) Wang, B.; Chen, Y.; Wu, Y.; Weng, B.; Liu, Y.; Lu, Z.; Li, C. M.; Yu, C. Aptamer Induced Assembly of Fluorescent Nitrogen-doped Carbon Dots on Gold Nanoparticles for Sensitive Detection of AFB_1. *Biosens. Bioelectron.* **2016**, *78*, 23−30.
(53) Zhang, N.; Li, X.; Ye, H.; Chen, S.; Ju, H.; Liu, D.; Lin, Y.; Ye, W.; Wang, C.; Xu, Q.; et al. Oxide Defect Engineering Enables to Couple Solar Energy into Oxygen Activation. *J. Am. Chem. Soc.* **2016**, *138*, 8928−8935.
(54) Zhang, B.; Wang, L.; Zhang, Y.; Ding, Y.; Bi, Y. Ultrathin FeOOH Nanolayers with Abundant Oxygen Vacancies on $BiVO_4$ Photoanodes for Efficient Water Oxidation. *Angew. Chem., Int. Ed.* **2018**, *57*, 2248−2252.
(55) Guo, D. Y.; Wu, Z. P.; An, Y. H.; Guo, X. C.; Chu, X. L.; Sun, C. L.; Li, L. H.; Li, P. G.; Tang, W. H. Oxygen Vacancy Tuned Ohmic-Schottky Conversion for Enhanced Performance in β-Ga_2O_3 Solar-Blind Ultraviolet Photodetectors. *Appl. Phys. Lett.* **2014**, *105*, 023507.
(56) Li, S.; Yue, J. Y.; Ji, X. Q.; Lu, C.; Yan, Z. Y.; Li, P. G.; Guo, D. Y.; Wu, Z. P.; Tang, W. H. Oxygen Vacancies Modulating the Photodetector Performances in Epsilon-Ga_2O_3 thin films. *J. Mater. Chem. C* **2021**, *9*, 5437−5444.
(57) Qian, L.-X.; Wu, Z.-H.; Zhang, Y.-Y.; Lai, P. T.; Liu, X.-Z.; Li, Y.-R. Ultrahigh-Responsivity, Rapid-Recovery, Solar-Blind Photodetector Based on Highly Nonstoichiometric Amorphous Gallium Oxide. *ACS Photonics* **2017**, *4*, 2203−2211.
(58) Ghaffarzadeh, K.; Nathan, A.; Robertson, J.; Kim, S.; Jeon, S.; Kim, C.; Chung, U. I.; Lee, J.-H. Persistent Photoconductivity in Hf-In-Zn-O Thin Film Transistors. *Appl. Phys. Lett.* **2010**, *97*, 143510.
(59) Lany, S.; Zunger, A. Anion Vacancies as a Source of Persistent Photoconductivity in II-VI and Chalcopyrite Semiconductors. *Phys. Rev. B* **2005**, *72*, 035215.
(60) Zhu, Q.; Xie, C. S.; Li, H. Y.; Zeng, D. W. A Method for Modeling and Deciphering the Persistent Photoconductance and Long-Term Charge Storage of ZnO Nanorod Arrays. *Nano Res.* **2016**, *9*, 2972−3002.
(61) Nguyen, D. A.; Oh, H. M.; Duong, N. T.; Bang, S.; Yoon, S. J.; Jeong, M. S. Highly Enhanced Photoresponsivity of a Monolayer WSe_2 Photodetector with Nitrogen-Doped Graphene Quantum Dots. *ACS Appl. Mater. Interfaces* **2018**, *10*, 10322−10329.
(62) Jin, B.; Cho, Y.; Zhang, Y.; Chun, D. H.; Li, P.; Zhang, K.; Lee, K.-S.; Park, J. H. A "Surface Patching" Strategy to Achieve Highly Efficient Solar Water Oxidation Beyond Surface Passivation Effect. *Nano Energy* **2019**, *66*, 104110.
(63) Dong, R.; Fang, Y. J.; Chae, J.; Dai, J.; Xiao, Z. G.; Dong, Q. F.; Yuan, Y. B.; Centrone, A.; Zeng, X. C.; Huang, J. S. High-Gain and Low-Driving-Voltage Photodetectors Based on Organolead Triiodide Perovskites. *Adv. Mater.* **2015**, *27*, 1912−1918.

https://doi.org/10.1021/acsami.2c15946
ACS Appl. Mater. Interfaces 2022, 14, 48936−48947